Soluble klotho binds monosialoganglioside to regulate membrane microdomains and growth factor signaling

George Dalton[a,1], Sung-Wan An[a,1], Saif I. Al-Juboori[b,1], Nicole Nischan[c], Joonho Yoon[a], Evgenia Dobrinskikh[d], Donald W. Hilgemann[e], Jian Xie[a], Kate Luby-Phelps[f,g], Jennifer J. Kohler[c], Lutz Birnbaumer[h,i,2], and Chou-Long Huang[a,2]

[a]Department of Medicine, University of Texas Southwestern Medical Center, Dallas, TX 75390; [b]Department of Electrical Engineering, University of Colorado Denver, Denver, CO 80204; [c]Department of Biochemistry, University of Texas Southwestern Medical Center, Dallas, TX 75390; [d]Department of Medicine, University of Colorado Denver, Denver, CO 80204; [e]Department of Physiology, University of Texas Southwestern Medical Center, Dallas, TX 75390; [f]Department of Cell Biology, University of Texas Southwestern Medical Center, Dallas, TX 75390; [g]Live Cell Imaging Core Facility, University of Texas Southwestern Medical Center, Dallas, TX 75390; [h]Neurobiology Laboratory, National Institute of Environmental Health Sciences, Research Triangle Park, NC 27709; and [i]Institute of Biomedical Research, School of Medical Sciences, Catholic University of Argentina, C1107AAZ Buenos Aires, Argentina

Soluble klotho, the shed ectodomain of the antiaging membrane protein α-klotho, is a pleiotropic endocrine/paracrine factor with no known receptors and poorly understood mechanism of action. Soluble klotho down-regulates growth factor-driven PI3K signaling, contributing to extension of lifespan, cardioprotection, and tumor inhibition. Here we show that soluble klotho binds membrane lipid rafts. Klotho binding to rafts alters lipid organization, decreases membrane's propensity to form large ordered domains for endocytosis, and down-regulates raft-dependent PI3K/Akt signaling. We identify α2-3-sialyllactose present in the glycan of monosialogangliosides as targets of soluble klotho. α2-3-Sialyllactose is a common motif of glycans. To explain why klotho preferentially targets lipid rafts we show that clustering of gangliosides in lipid rafts is important. In vivo, raft-dependent PI3K signaling is up-regulated in klotho-deficient mouse hearts vs. wild-type hearts. Our results identify ganglioside-enriched lipid rafts to be receptors that mediate soluble klotho regulation of PI3K signaling. Targeting sialic acids may be a general mechanism for pleiotropic actions of soluble klotho.

soluble klotho | lipid rafts | gangliosides | sialic acids | TRPC6

Mice homozygous for a severe hypomorphic α-*klotho* allele manifest multiple aging-related phenotypes and die prematurely at 2–3 mo after birth (1). α-Klotho is predominantly expressed in renal tubules, parathyroid glands, and epithelial cells of the choroids plexus, but not in myocardium. Overexpression of α-klotho extends life span in mice, indicating that it is an aging-suppression molecule (2). The full-length α-klotho protein is a single-pass membrane protein with a large extracellular domain, a membrane-spanning segment, and a short intracellular carboxyl terminus (1). Membranous α-klotho associates with FGF receptors to form coreceptors for the ligand FGF23, a bone-derived circulating hormone that plays an important role in phosphate homeostasis (3).

The ectodomain of α-klotho, ~950 aa in length, is composed of two internal repeats, KL1 and KL2, each sharing amino acid sequence homology to family-1 glycosidases (4). The ectodomain (soluble klotho, sKL) is released into the systemic circulation, urine, and cerebrospinal fluid and functions as a humoral factor (2, 5). To date, more than 10 different functions of sKL have been described (2, 6–9). sKL regulates ion transporters, antagonizes Wnt and TGF-β1signaling to suppress cellular senescence, tissue fibrosis, and cancer metastasis, and inhibits insulin and insulin-like growth factor-1 (IGF1)-driven PI3K/Akt signaling contributing to extension of lifespan in mice, cardioprotection, and inhibition of tumor cell proliferation. A fundamental gap in the understanding of sKL's mechanism of action is the lack of knowledge of potential membrane receptor(s) that mediate cellular responses to sKL.

Lipid rafts are highly dynamic, cholesterol- and sphingolipid-rich membrane microdomains that compartmentalize cellular processes such as signal transduction and membrane trafficking (10). Lateral association of sphingolipids and cholesterol in the outer leaflet driven by the preferential affinity of sphingolipids toward one another and toward cholesterol governs the spontaneous formation of lipid rafts. Here, we show that sKL binds lipid rafts and identify α2-3-sialyllactoses of monosialogangliosides, GM1 and GM3, as targets. Klotho binding to lipid rafts alters lipid organization and down-regulates raft-dependent PI3K signaling. Sialyllactoses are common motifs of glycans present in many glycoproteins as well as gangliosides (11). We further show that clustering of gangliosides in lipid rafts enhances the affinity for sKL and demonstrate that sKL preferentially targets raft-associated gangliosides vs. isolated gangliosides in nonraft membranes. To demonstrate the in vivo relevance, we show that lipid raft-dependent PI3K/Akt signaling is up-regulated in hearts isolated from klotho-deficient vs. wild-type mice. Our results reveal sKL to be a physiological regulator of lipid raft formation and function and provide a potential general mechanism for pleiotropic actions of sKL.

Significance

Soluble klotho is the shed ectodomain of the antiaging membrane protein α-klotho that exhibits pleiotropic actions, including down-regulation of growth factor-driven PI3K signaling, contributing to lifespan prolongation, cardioprotection, and tumor inhibition. Whether membrane receptors exist for soluble klotho is unknown. We identify lipid rafts as receptors for soluble klotho. We show klotho binds specific sialic acid residues of gangliosides highly enriched in the outer leaflet of lipid rafts. Klotho binding to gangliosides modulates lipid organization and inhibits lipid raft-dependent PI3K signaling. In vivo, klotho-deficient mouse hearts have heightened raft-dependent PI3K signaling vs. wild-type hearts. We reveal a novel physiological regulator of lipid raft structure and function, and open new research to understand pleiotropic effects of klotho in cell signaling and metabolism.

Results

sKL Binds Lipid Rafts and Modulates Lipid Organization Within Rafts.

sKL is pleiotropic. We posit that multifunctional lipid rafts may be receptors for sKL. sKL comigrated with markers of lipid rafts (Fig. 1A), indicating affinity for isolated lipid rafts. To examine whether klotho binds lipid rafts in intact cells and the potential effects of binding, we used colocalization analysis of two different fluorophore-labeled gangliosides in cell membranes. HeLa cells were stained with CTxB-Alexa Fluor-594 conjugate (to label endogenous GM1) followed by exogenous BODIPY-FL-C_5-GM1 and imaged by dual-color confocal microscopy. Correlation between pixel intensity histogram of CTxB-labeled red channel and BODIPY-GM1 green channel was analyzed by Pearson's correlation (coefficient values "1" and "0" correspond to perfect colocalization and completely random uncorrelated distribution, respectively). As shown, mean Pearson's coefficient ($p.c.$) for CTxB-labeled GM1 and BODIPY-GM1 is 0.53 ± 0.02 (Fig. 1 B

and C; $P < 0.001$ vs. 0), indicating highly significant colocalization. Disrupting lipid rafts by methyl-β-cyclodextrin (MβCD) markedly reduced $p.c.$ for CTxB and BODIPY-GM1 to a value not significantly different from 0, supporting that the two fluorescence-labeled gangliosides are highly colocalized in lipid rafts (Fig. 1B and Fig. S1A). Caveolin-1, a marker for lipid rafts, also showed significant colocalization with CTxB, whereas the non-raft protein CD71 (transferrin receptor) did not show colocalization with CTxB (Fig. 1B and Fig. S1 B and C). Treatment with sKL markedly decreased $p.c.$ for CTxB and BODIPY-GM1 (Fig. 1B and Fig. S1D; see Fig. S1 legend for comments).

The resolution of confocal microscopy is limited by the diffraction of light to ~250 nm. To support that klotho targets lipid rafts, we conducted Förster resonance energy transfer (FRET) studies. FRET detects molecular interactions on a scale of 1–10 nm, smaller than the lowest size limit of rafts (10–200 nm). FRET was measured by fluorescence lifetime imaging microscopy (FLIM) and analyzed by the phasor approach (12). As a control, lifetime for
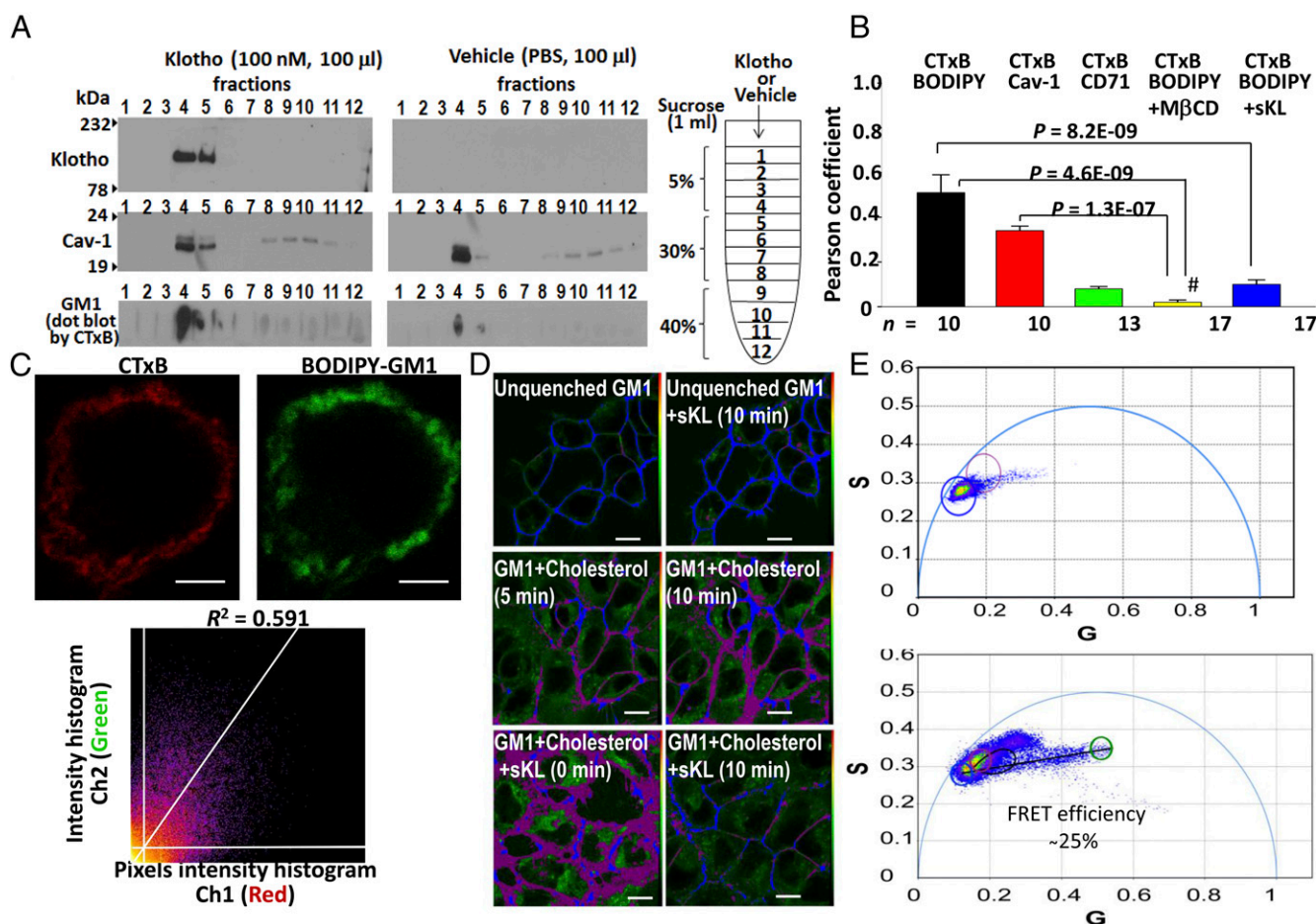
Fig. 1. Klotho binds lipid rafts and alters lipid organization. (A) Purified sKL was layered on top of HeLa cell lysates and fractioned by sucrose-density gradient centrifugation. An equal volume from each fraction was acetone-precipitated and analyzed for klotho, caveolin-1, and protein-associated GM1. (B) Cells were incubated with CTxB and BODIPY-GM1 at 4 °C to prevent endocytosis. Cells were treated with klotho (300 pM, 10 min) or MβCD (10 mM, 30 min) at 37 °C before CTxB and BODIPY-GM1. Data are mean ± SEM (n = 10–17 images as indicated for each group). (C) Representative images and Pearson's correlation analysis of colocalization between CTxB and BODIPY-GM1. The scatterplot shows a 2D intensity histogram of the red and green pixels in the image. Pixels with intensity above the thresholds (indicated for each channel by the white lines) are colocalized. Pearson's correlation coefficient (R^2) for the colocalized volume = 0.591. (Scale bars, 5 μm.) (D) Cells were stained with BODIPY FL-505/510-C_5-GM1 (donor) with or without CholEsteryl BODIPY 542/563-C_{11} (acceptor), excited with a two-photon laser at 900 nm, and emission was collected at 506–594 nm using FLIM. Merged intensity images (showing green BODIPY-GM1 with some internalization) and pseudocolor lifetime images are shown. Experiments were performed four times with similar results. (Scale bars, 10 μm.) (E) Phasor plot of fluorescence lifetime histogram from cells stained with GM1 only (Top) and the trajectory of FRET between GM1 and cholesterol (Bottom). Blue circle marks lifetime for donor only, purple circle for donor + acceptor, and green circle for background autofluorescence (from unstained cells). Phasor plot analysis showed FRET efficiency ~25%, with fractional contribution of lifetimes ~51% from quenched donor, 44% from unquenched donor, and 5% from background.

GM1 (donor) in the absence of cholesterol (acceptor) has longer values, and sKL treatment did not affect lifetime for GM1 alone (Fig. 1D, *Top*; blue color ≈ longer lifetime values). Lifetime for GM1 shifted to the shorter values (purple) in the presence of cholesterol, indicating quenching of GM1 by cholesterol (i.e., FRET occurrence between GM1 and cholesterol; Fig. 1D, *Middle*). Klotho treatment decreased FRET between GM1 and cholesterol – lifetime for GM1 shifted back to the longer values (Fig. 1D, *Bottom*). Phasor plot analysis supported the validity of FLIM-FRET data (Fig. 1E). The results indicate that klotho treatment decreased FLIM-FRET occurrences between GM1 and cholesterol, supporting an effect of klotho binding on lipid organization within rafts. Lipid rafts feature a high degree of membrane order. sKL decreases membrane order (*SI Text* and Fig. S2), further supporting that it binds lipid rafts to modulate lipid organization.

Klotho Selectively Down-Regulates Lipid Raft-Dependent PI3K/Akt Signaling and Thereby Inhibits TRPC6 Channel Function. sKL inhibits growth factor (GF)-driven PI3K signaling (2, 9). PI3K is present in lipid rafts and in nonraft membranes depending on context (13). Supporting that lipid rafts are receptors for sKL and mediate its effect to inhibit PI3K signaling, sKL treatment down-regulated PI3K/Akt signaling associated with lipid rafts (fractions 4 and 5, marked by caveolin-1), but not in nonraft regions (fractions 9–12; Fig. 2 A and B). The specificity of sKL on lipid raft-dependent, GF-driven PI3K/Akt signaling is further evidenced by findings that whereas IGF1 restored PI3K/Akt signaling in raft and nonraft regions after its down-regulation by serum starvation, klotho treatment only affected IGF1-stimulated PI3K/Akt signaling in the rafts (Fig. S3). For comparison, pharmacological inhibition of

PI3K by wortmannin (Wmn) abrogated PI3K/Akt signaling in both raft and nonraft regions (Fig. S3; see legend for comments).

sKL inhibits PI3K-dependent diacylglycerol (DAG)-stimulated exocytosis of TRPC6 channels, underlying its cardioprotective action (9). TRPC6 channel is activated by DAG via dual mechanisms: (*i*) direct activation of channel gating and (*ii*) stimulation of channel exocytosis (Fig. 3A and refs. 14 and 15). We used DAG-stimulated TRPC6 function as an additional experimental system to study the regulation of PI3K signaling by sKL. As reported before, klotho inhibited DAG-stimulated TRPC6 currents, an effect not additive to the effect of Wmn or to tetanus toxin (TTX)-mediated blocking of channel exocytosis (Fig. 3B). Because klotho down-regulates PI3K signaling to inhibit DAG-stimulated TRPC6 exocytosis but does not affect direct channel gating by DAG, the maximal inhibition of TRPC6 by klotho is only partial (Fig. 3 A and B). Treatment with the cholesterol binder filipin decreased DAG-stimulated TRPC6 currents and prevented further inhibition of currents by klotho (Fig. 3C). There was no additivity among inhibition of TRPC6 caused by klotho, filipin, TTX, and Wmn (Fig. 3C, *Inset* and Fig. S4). Thus, lipid rafts mediate down-regulation of PI3K-dependent TRPC6 exocytosis by sKL. Inhibition of TRPC6 by klotho was reversed after klotho washout (Fig. S5).

Sphingolipids including gangliosides are important components of lipid rafts. Pretreatment of cells with N-butyldeoxy-ygalactonojirimycin (NB-DGJ), which blocks biosynthesis of gangliosides (16), decreased DAG-stimulated TRPC6 currents and prevented further decreases by sKL (Fig. 3 D and E). Specificity of NB-DGJ–mediated depletion of membrane gangliosides is supported by findings that application of exogenous GM1, but not asialo-GM1 (a GM1 analog missing sialic acid), reversed NB-DGJ–induced decreases of TRPC6 currents to the control level without NB-DGJ (Fig. 3E). In cells rescued from the effect of NB-DGJ by GM1, klotho treatment decreased TRPC6 currents. GM3 is a more abundant monosialoganglioside than GM1 in many nonneuronal tissues (17). Thus, we examined the role of GM3. Exogenous GM3, but not lactosylceramide (LacCer; a GM3 analog missing sialic acid), also reversed the inhibition of TRPC6 caused by NB-DGJ and restored the effect of klotho to inhibit TRPC6 after NB-DGJ (Fig. 3F). Thus, gangliosides and cholesterol-enriched lipid rafts mediate klotho regulation of PI3K signaling and TRPC6 function.

Klotho Specifically Targets α2-3-Sialyllactose in the Glycan of Gangliosides to Regulate Lipid Rafts. Lipid rafts also contain glycoproteins with α2-3-sialic acid in the glycan structure. We next address whether sKL targets α2-3-sialic acids present in gangliosides or in raft-associated glycoproteins to regulate TRPC6 function, by using disialoganglioside GD3 that has an additional α2-8-sialic acid linkage to the underlying α2-3-sialic acid (Fig. 3D). Exogenous GD3 rescued PI3K-dependent TRPC6 activity after inhibition by NB-DGJ (Fig. 3G), indicating it can substitute endogenous gangliosides for klotho regulation of TRPC6. Interestingly, klotho treatment failed to inhibit TRPC6 in cells rescued by GD3 after NB-DGJ. The fact that whereas both GD3 and GM3 rescue TRPC6 currents klotho only inhibited TRPC6 in cells rescued by GM3, but not by GD3, indicates that klotho targets exposed α2-3–linked sialic acid in gangliosides, rather than α2-8–linked sialic acid. Because glycoproteins in lipid rafts are not expected to be different in GD3-rescued vs. GM3-rescued cells, the results argue against klotho's targeting α2-3-sialic acid–containing glycoproteins.

This notion is further extended by competition experiments. When preincubated with GM1, but not asialo-GM1, klotho failed to inhibit TRPC6 (Fig. S6A). Moreover, preincubation with GM3, but neither LacCer nor GD3, neutralized the ability of klotho to inhibit TRPC6 (Fig. S6 A–C). Inability of GD3 to neutralize the effect of klotho lends additional support to the
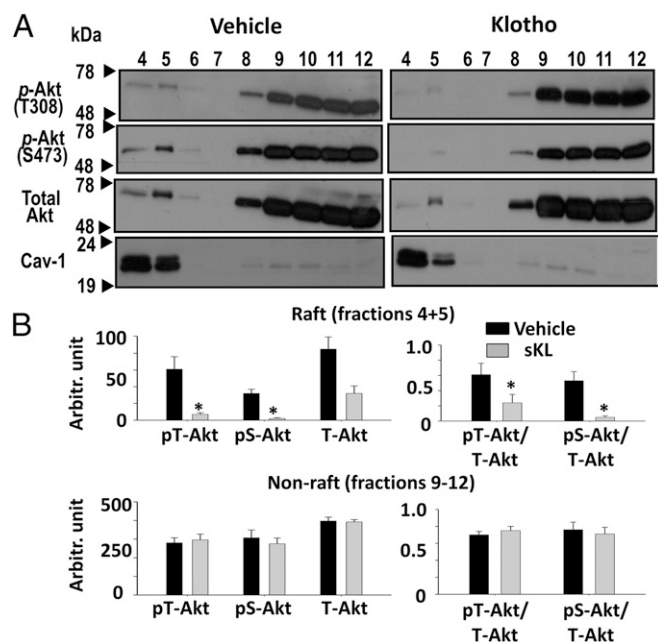
Fig. 2. Klotho inhibits lipid raft-associated PI3K signaling. (A and B) HeLa cells in serum-containing medium were treated with sKL before lysis in an ice-cold detergent lysis buffer containing 1% Triton X-100 and subjected to sucrose gradient ultracentrifugation. pT-Akt, phosphorylation of Akt at Thr-308; pS-Akt, at Ser-473. T-Akt indicates total Akt. A shows one representative experiment. B shows mean ± SEM from four separate experiments. Intensity values were determined from densitometry. Ratios of phospho-Akt over total Akt (pT-Akt/T-Akt, pS-Akt/T-Akt) are also shown. *P < 0.01, sKL vs. vehicle.
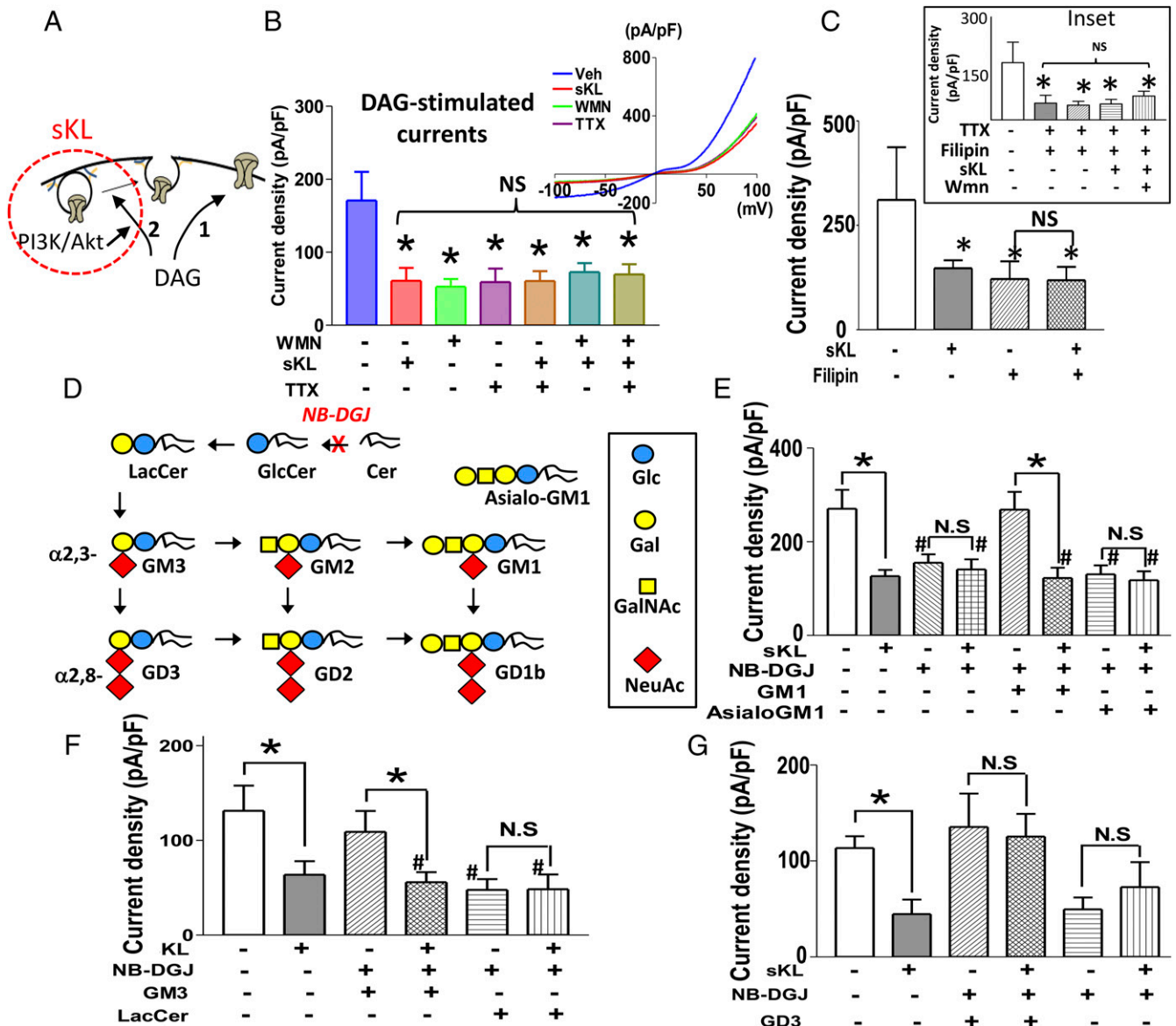
Fig. 3. Klotho inhibits PI3K-dependent DAG-stimulated exocytosis of TRPC6. (*A*) Diagram illustrating dual effects of DAG on TRPC6. (*B*) *Inset* shows current-voltage (I-V) relationship for DAG-stimulated currents. OAG (a membrane-permeant analog of DAG, 100 μM) was used to activate TRPC6. Data are mean ± SEM of maximal DAG-stimulated inward TRPC6 current density (Δ current ± DAG in pA at −100 mV divided by cell capacitance in picofarads). *P < 0.01 vs. control (first bar from left). n = 8–12 each group. sKL (300 pM for 3 h); Wmn (200 nM for 20 min); TTX (50 nM for 3 h). (*C*) No additivity among inhibition of TRPC6 by sKL, filipin (2 μg/mL for 1 h), TTX, and Wmn. *P < 0.01 vs. control (first bar from left). n = 9–12 each group. (*D*) Diagram for metabolic pathway of some gangliosides pertinent in this study. NB-DGJ blocks glucosylation of ceramide, the entry step of ceramide biosynthesis into gangliosides. (*E*) Cells were treated with NB-DGJ (25 μM) for 7 h, then together with exogenous GM1 or asialo-GM1 (10 μM each) for additional 19 h. After removing medium containing both, cells were treated with sKL in a new medium for 3 h before recording. n = 10–13 each group. *P < 0.01 between indicated groups. #P < 0.01 vs. control (first bar from left). (*F*) Experiment as in *E* except exogenous GM3 or LacCer (10 μM each) was used. n = 12–14 each group. *P < 0.01 between indicated groups. #P < 0.01 vs. control (first bar from left). (*G*) Experiment as in *E* except exogenous GD3 (10 μM) was used. n = 10–13 each group. *P < 0.01 between indicated groups. NS, not significant.

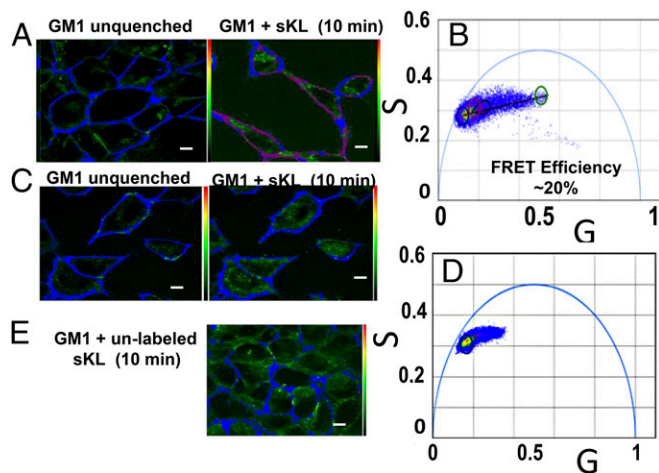finding in Fig. 3*G* that accessibility of α2-3–linked sialic acid is critical for klotho binding. Together, the results in Fig. 3*G* and Fig. S6 *A*–*C* point to the structure of GM3 glycan, α2-3-sialyllactose (Neu5Acα2-3Galβ1-4Glc; also known as 3′-sialyllactose), as the minimal motif for klotho binding and regulation of TRPC6. Indeed, 3′-sialyllactose at a concentration (3 mM) much higher than that for GM1 and GM3 in the above experiments (10 μM) fully neutralized the effect of klotho, whereas lactose at the same concentration had no effect (Fig. S6*D*). The apparent K_d for GM3 binding to klotho, based on IC_{50} for competing klotho inhibition of TRPC6, is ∼3 μM (Fig. S6*E*). The apparent K_d

determined similarly for 3′-sialyllactose binding to klotho is ∼1 mM (Fig. S6*F*) and agrees with the K_d for 3′-sialyllactose binding with sialic acid-binding Ig-like lectin (Siglec) family proteins (18). GM3 forms micelles in solution, likely explaining differences in the apparent K_d for GM3 vs. free 3′-sialyllactose (*Discussion*). α2-6-Sialyllactose (Neu5Acα2–6Galβ1-4Glc; also known as 6′-sialyllactose) also competed for klotho's effect although with slightly less efficacy than 3′-sialyllactose (Fig. S7). Next, we used biolayer interferometry to analyze binding of klotho to 3′-sialyllactose in vitro. Klotho bound to streptavidin-immobilized biotin-labeled 3′-sialyllactose, but not to lactose (Fig. S6 *G* and *H*). K_d for the
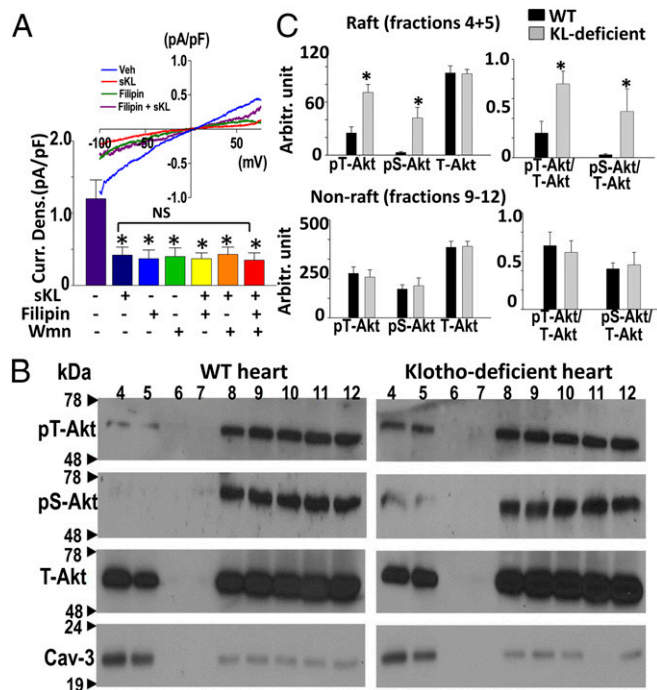
binding is estimated ~40 nM. High density of 3′-sialyllactose immobilized on the binding surface likely explains the apparently higher binding affinity of klotho determined by this method.

Klotho Binds Lipid Rafts in Live Cells by Interacting with Raft-Associated GM1. To further support that klotho indeed binds to monosialogangliosides clustered in lipid rafts, we examined klotho interaction with GM1 in live cells by studying FRET between fluorophore-labeled klotho and BODIPY-GM1. Addition of fluorophore-labeled klotho causes fluorescence quenching of cell membrane BODIPY-GM1 analyzed by FLIM-FRET in 10 min (Fig. 4 *A* and *B*), indicating klotho and GM1 interact within a 10-nm distance. In cells pretreated with MβCD to disrupt lipid rafts, BODIPY-GM1 remained partitioned into cell membranes, but addition of fluorophore-labeled klotho failed to quench GM1 fluorescence (Fig. 4 *C* and *D*). As a control, addition of unlabeled klotho to normal cells did not cause quenching of BODIPY-GM1 (Fig. 4*E*). The results provide direct evidence to support that klotho targets raft-associated GM1. In addition, klotho prevents cells from forming large ordered domains but does not cause global membrane disorder (*SI Text* and Fig. S8).

Evidence for Effect of sKL on Lipid Rafts in Vivo. Cardioprotection by klotho is mediated by circulating sKL through down-regulating PI3K-dependent activation of TRPC6 channels (9). To investigate the role of klotho on lipid rafts in vivo, we first showed that lipid rafts mediate sKL's effect to down-regulate PI3K-dependent TRPC6 channel function in freshly isolated cardiac myocytes: Filipin, Wmn, and klotho each decreased TRPC6-mediated currents by a similar degree, and the combined effects

Fig. 5. Evidence for klotho down-regulation of lipid raft-associated PI3K signaling in vivo. (*A*) DAG-stimulated TRPC6 currents were recorded in ventricular myocytes isolated from mice after isoproterenol overstimulation to induce TRPC6 surface expression (9). Data are mean ± SEM of inward current density. *n* = 10–13 each group. *P < 0.01 vs. control (first bar from left). (*B* and *C*) Raft-associated PI3K/Akt signaling (marked by caveolin-3) is up-regulated in klotho-deficient mouse hearts vs. wild-type mouse hearts. Hearts isolated from wild-type or homozygous *klotho* knockout mice were homogenized, lysed in ice-cold 1% Triton X-100 buffer, and subjected to sucrose gradient ultracentrifugation. *B* shows one representative experiment. *C* shows mean ± SEM from four separate experiments. *P < 0.01, wild-type vs. klotho-deficient hearts.

from individual agents were not additive (Fig. 5*A*). Together with the recent report that TRPC6 is localized to lipid rafts of isolated myocytes (19), the results support that raft-dependent PI3K signaling in the heart is a useful readout for in vivo effects of sKL on lipid rafts. We then compared raft-associated PI3K signaling in klotho-deficient hearts vs. wild-type hearts. Raft-dependent PI3K signaling was significantly up-regulated in klotho-deficient hearts (from mice rescued from death by dietary phosphate restriction) compared with wild-type hearts (Fig. 5 *B* and *C*). The increase in PI3K signaling was restricted to lipid rafts; no differences in PI3K signaling were observed in nonraft membranes between klotho-deficient and wild-type hearts. Thus, circulating sKL plays an important role in regulating lipid rafts in vivo.

Discussion

Monosialogangliosides are dynamically distributed between raft and nonraft membranes as lipid rafts undergo self-assembly and disassembly. sKL normally circulates at very low levels (30–100 pM) (2). The low affinity of sKL for α2-3-sialyllactose (K_d ~1 mM) suggests that isolated α2-3-sialyllactose monomers in nonraft membranes may not be effective physiological targets of sKL. Glycan clustering is a common mechanism for enhancing binding of low-affinity glycans to multivalent glycan-binding proteins (11). sKL is likely multivalent due to the fact that sKL forms dimers and each unit contains two highly homologous KL1 and KL2 domains with potential glycan-binding activity (4, 20). Results of in vitro binding assays and competition experiments using TRPC6-based functional assays show that the apparent

Fig. 4. Klotho–GM1 interaction live cell membranes analyzed by FLIM-FRET. (*A*) HEK cells were stained with BODIPY FL-505/510-C5-GM1 (donor; 100 nM). Lifetime for GM1 alone has longer values (blue color cursor ≈ regions with longer lifetime values). Lifetime for GM1 shifted to the shorter values (purple color cursor) in the presence of fluorophore-labeled sKL (acceptor; 300 pM) over 10 min, indicating quenching of GM1 by sKL and FLIM-FRET occurrence between GM1 and klotho. (*B*) Phasor plot analysis of FLIM-FRET data showed FRET efficiency ~20%, with fractional contribution of lifetimes ~36% from quenched donor, 55% from unquenched donor, and 9% from background. In the trajectory, blue circle marks lifetime for donor plus unlabeled klotho, purple circle for donor plus labeled klotho, and green circle for background autofluorescence. (*C* and *D*) Cells were pretreated with 5 mM MβCD for 3 h at 37 °C to disrupt lipid rafts. GM1 lifetime after addition of fluorophore-labeled sKL was comparable to GM1 only, indicating little to no FRET occurrence between GM1 and klotho. Shown is representative of three separate experiments with similar findings. (*E*) Addition of unlabeled klotho does not cause shift to shorter values (vs. *A*), indicating no quenching of BODIPY-GM1 fluorescence by unlabeled klotho. (Scale bars, 5 μm in *A*, *C*, and *E*.)

Dalton et al.

binding affinity of sKL for clustered α2-3-sialyllactoses is >300-fold higher than for free α2-3-sialyllactoses, strongly supporting the notion that lipid rafts highly enriched in α2-3-sialyllactose–containing gangliosides are effective physiological targets of sKL. The notion of selective targeting of sKL to lipid rafts is further supported by FRET experiments in live cells showing that klotho selectively interacts with raft-associated GM1, and by experiments using the highly sensitive electric probe C6TPP showing that sKL does not affect disordered membranes that reflect nonraft membrane regions (Fig. S8). Moreover, raft-dependent PI3K signaling is selectively up-regulated in klotho-deficient hearts compared with wild-type hearts. The precise stoichiometry of klotho subunits and sialyllactose motifs required for effective binding in vivo remains to be determined.

Local lipid and protein interactions and interactions of raft proteins or lipids with cortical actin cytoskeleton play important roles in lipid raft formation (10, 21). Physiological soluble factors that control the formation and function of lipid rafts are much less known. We identify sKL as a physiological circulating regulator of lipid rafts by targeting sialogangliosides. Physiological levels of sKL likely modulate the function of lipid rafts acting as a rheostat rather than as an on–off switch. Interestingly, a recent paper reports that soluble FLT1 (the shed ectodomain of VEGF receptors) also regulates podocyte function by binding to GM3 in lipid rafts (22). We have also found that klotho is expressed in podocytes and protects podocytes against injury (23). Thus, gangliosides-enriched lipid rafts are important targets of extracellular factors with potentially important biological and disease significance.

sKL is a pleiotropic hormone with poorly understood mechanism of action (2, 6–9). Lipid rafts may mediate multiple cellular effects of sKL. The physiological effect of klotho through targeting sialic acid, however, is not limited to glycolipids. Previously, we showed that sKL targets terminally exposed α2-6-sialic acids in the N-glycan of TRPV5 to prevent its endocytosis via caveolae (24). Here, we show that α2-3-sialyllactose also binds klotho, supporting that klotho targets both α2-3– and α2-6–linked sialic acids. Klotho's effect on N-glycans of TRPV5 is different from that on lipid rafts. Klotho's effect on lipid rafts is reversible on washout. Further, the effect of klotho on TRPC6 function is mediated by raft-dependent PI3K/Akt signaling, whereas klotho acts directly on the TRPV5 channel protein (9, 24, 25). Regarding klotho's effect on α2-6-sialyllactose of TRPV5 N-glycans, the binding affinity may be enhanced by the channel's tetrameric structure and concentration in caveolae. Ultimately, the crystal structure of klotho will help elucidate the molecular basis of klotho's specificity for α2-3- and α2-6-sialic acid and the role of underlying lactose.

In summary, sialic acids in the context of α2-3- or α2-6-sialyllactose are low-affinity targets of sKL. Through enrichment of gangliosides containing terminal α2-3-sialyllactoses, lipid rafts form effective binding sites for physiologically low circulating levels of sKL. sKL binding to lipid rafts modulates lipid organization and down-regulates PI3K signaling, perhaps by affecting function of raft-associated GF receptors and/or recruitment of PI3K to rafts or its activity.

Materials and Methods

Expanded methods are available in SI Materials and Methods. Animal use was approved by the institutional animal care and use committee of the University of Texas Southwestern Medical Center.

Lipid rafts were fractioned by sucrose gradient ultracentrifugation. Confocal imaging of fluorophore-labeled CTxB, GM1, cholesterol, and FLIM-FRET studies were performed using a Zeiss LSM510 laser scanning confocal microscope system. GP studies were performed by staining cells with Di-4-ANEPPDHQ. Binding studies were performed using biolayer interferometry. Whole-cell patch-clamp recording was performed in HEK or HeLa cells transfected with TRPC6 plasmid.

1. Kuro-o M, et al. (1997) Mutation of the mouse klotho gene leads to a syndrome resembling ageing. *Nature* 390(6655):45–51.
2. Kurosu H, et al. (2005) Suppression of aging in mice by the hormone Klotho. *Science* 309(5742):1829–1833.
3. Kurosu H, et al. (2006) Regulation of fibroblast growth factor-23 signaling by klotho. *J Biol Chem* 281(10):6120–6123.
4. Ito S, Fujimori T, Hayashizaki Y, Nabeshima Y (2002) Identification of a novel mouse membrane-bound family 1 glycosidase-like protein, which carries an atypical active site structure. *Biochim Biophys Acta* 1576(3):341–345.
5. Imura A, et al. (2004) Secreted Klotho protein in sera and CSF: Implication for posttranslational cleavage in release of Klotho protein from cell membrane. *FEBS Lett* 565(1-3):143–147.
6. Huang CL, Moe OW (2011) Klotho: A novel regulator of calcium and phosphorus homeostasis. *Pflugers Arch* 462(2):185–193.
7. Zhou L, Li Y, Zhou D, Tan RJ, Liu Y (2013) Loss of Klotho contributes to kidney injury by derepression of Wnt/β-catenin signaling. *J Am Soc Nephrol* 24(5):771–785.
8. Liu H, et al. (2007) Augmented Wnt signaling in a mammalian model of accelerated aging. *Science* 317(5839):803–806.
9. Xie J, et al. (2012) Cardioprotection by Klotho through downregulation of TRPC6 channels in the mouse heart. *Nat Commun* 3:1238.
10. Simons K, Sampaio JL (2011) Membrane organization and lipid rafts. *Cold Spring Harb Perspect Biol* 3(10):a004697.
11. Cohen M, Varki A (2014) Modulation of glycan recognition by clustered saccharide patches. *Int Rev Cell Mol Biol* 308:75–125.
12. Digman MA, Caiolfa VR, Zamai M, Gratton E (2008) The phasor approach to fluorescence lifetime imaging analysis. *Biophys J* 94(2):L14–L16.
13. Gao X, et al. (2011) PI3K/Akt signaling requires spatial compartmentalization in plasma membrane microdomains. *Proc Natl Acad Sci USA* 108(35):14509–14514.
14. Hofmann T, et al. (1999) Direct activation of human TRPC6 and TRPC3 channels by diacylglycerol. *Nature* 397(6716):259–263.
15. Cayouette S, Lussier MP, Mathieu EL, Bousquet SM, Boulay G (2004) Exocytotic insertion of TRPC6 channel into the plasma membrane upon Gq protein-coupled receptor activation. *J Biol Chem* 279(8):7241–7246.
16. Andersson U, Butters TD, Dwek RA, Platt FM (2000) N-butyldeoxygalactonojirimycin: A more selective inhibitor of glycosphingolipid biosynthesis than N-butyldeoxynojirimycin, in vitro and in vivo. *Biochem Pharmacol* 59(7):821–829.
17. Müthing J, Cacić M (1997) Glycosphingolipid expression in human skeletal and heart muscle assessed by immunostaining thin-layer chromatography. *Glycoconj J* 14(1):19–28.
18. May AP, Robinson RC, Vinson M, Crocker PR, Jones EY (1998) Crystal structure of the N-terminal domain of sialoadhesin in complex with 3′ sialyllactose at 1.85 A resolution. *Mol Cell* 1(5):719–728.
19. Makarewich CA, et al. (2014) Transient receptor potential channels contribute to pathological structural and functional remodeling after myocardial infarction. *Circ Res* 115(6):567–580.
20. Tucker Zhou TB, King GD, Chen C, Abraham CR; Tucker- Zhou (2013) Biochemical and functional characterization of the klotho-VS polymorphism implicated in aging and disease risk. *J Biol Chem* 288(51):36302–36311.
21. Gowrishankar K, et al. (2012) Active remodeling of cortical actin regulates spatiotemporal organization of cell surface molecules. *Cell* 149(6):1353–1367.
22. Jin J, et al. (2012) Soluble FLT1 binds lipid microdomains in podocytes to control cell morphology and glomerular barrier function. *Cell* 151(2):384–399.
23. Kim JH, et al. (2016) Klotho may ameliorate proteinuria by targeting TRPC6 channels in podocytes. *J Am Soc Nephrol* ASN.2015080888.
24. Cha SK, et al. (2008) Removal of sialic acid involving Klotho causes cell-surface retention of TRPV5 channel via binding to galectin-1. *Proc Natl Acad Sci USA* 105(28):9805–9810.
25. Chang Q, et al. (2005) The beta-glucuronidase klotho hydrolyzes and activates the TRPV5 channel. *Science* 310(5747):490–493.
26. Owen DM, Rentero C, Magenau A, Abu-Siniyeh A, Gaus K (2011) Quantitative imaging of membrane lipid order in cells and organisms. *Nat Protoc* 7(1):24–35.
27. Hilgemann DW, Fine M (2011) Mechanistic analysis of massive endocytosis in relation to functionally defined surface membrane domains. *J Gen Physiol* 137(2):155–172.
28. Lingwood D, Kaiser HJ, Levental I, Simons K (2009) Lipid rafts as functional heterogeneity in cell membranes. *Biochem Soc Trans* 37(Pt 5):955–960.
29. Waugh MG, Hsuan JJ (2009) Preparation of membrane rafts. *Methods Mol Biol* 462:403–414.
30. Degli Esposti M, et al. (2009) Fas death receptor enhances endocytic membrane traffic converging into the Golgi region. *Mol Biol Cell* 20(2):600–615.
31. Owen DM, et al. (2006) Fluorescence lifetime imaging provides enhanced contrast when imaging the phase-sensitive dye di-4-ANEPPDHQ in model membranes and live cells. *Biophys J* 90(11):L80–L82.

MEDICAL SCIENCES

Supporting Information

Dalton et al. 10.1073/pnas.1620301114

SI Text

Klotho Decreases Membrane Order Analyzed by Generalized Polarization.
The biophysical hallmark of lipid rafts is a high degree of membrane
order. We examined the effect of klotho on membrane order using a
polarity-sensitive membrane probe that undergoes an emission
spectral shift when residing in the liquid-ordered vs. disordered
phase (26). Generalized polarization (*GP*), the ratio of fluorescence
intensity recorded in two spec-tral channels, becomes increasingly
more negative within 5–10 min of klotho treatment, indicating de-
creasing membrane order (Fig. S2 *A* and *B*). The effect of klotho on
GP is reversible after klotho washout (Fig. S2*C*). Together, the
above results provide compelling support for the notion that klotho
binds to lipid rafts and that binding modulates lipid organization
within rafts.

**Klotho Prevents Cells from Forming Large Ordered Domains but Does
Not Cause Global Membrane Disorder.** Large intracellular Ca^{2+}
transients cause massive endocytosis (MEND) in many cell types
by inducing coalescence of ordered membrane domains (27).
Supporting that klotho binding to gangliosides hinders mem-
brane ordering, klotho treatment strongly reduced MEND in
HEK293 cells expressing Na^+/Ca^{2+} exchangers that are used to
generate Ca^{2+} transients (Fig. S8 *A* and *B*). Pretreatment with
NB-DGJ prevented the effect of sKL to reduce MEND, further
supporting the notion that the effect of klotho is due to binding
to gangliosides.

   To test further whether klotho binding causes global membrane
disorder, we used an electrogenic membrane probe hexyl-
triphenylphosphonium (C6TPP) that preferentially translocates
across the disordered membrane (28). Transmembrane current
carried by C6TPP is strongly increased by extracting cholesterol
from cells with cyclodextrins (27). As shown, the inward currents
generated by external application of C6TPP at three different
concentrations in HEK293 cells were unaffected by klotho treat-
ment (Fig. S8 *C* and *D*). Thus, the effects of klotho are specific to
a subset of membrane subdomains (i.e., lipid rafts) in the resting
state of cells. The fact that sKL is selective for lipid rafts and does
not cause global membrane disorder is consistent with its being a
physiological regulator of cell membrane function.

   Besides down-regulation of raft-dependent PI3K signaling,
klotho treatment also markedly reduces MEND triggered by large
Ca^{2+} influx. Both effects of sKL are mediated by klotho binding
to gangliosides, because they are prevented by depletion of
gangliosides. Depletion of gangliosides by NB-DGJ treatment,
however, does not affect MEND in itself. MEND is believed to
occur as a result of large coalescence of ordered domains leading
to phase separation in cell membranes (27). NB-DGJ depletes
gangliosides but does not affect the biosynthesis of ceramide and
sphingomyelin (Fig. 3*D*). Ceramide and sphingomyelin can
support the formation of lipid rafts (10, 28), explaining why
MEND is not affected by NB-DGJ. These results lend further
support for structural and functional heterogeneities of ordered
membrane microdomains and for the idea that sKL targets to
monosialoganglioside-enriched membrane subdomains.

SI Materials and Methods

Materials. MβCD was from Sigma-Aldrich. IGF1 and recombinant
human klotho protein were from R & D Systems. Cholera toxin
subunit B-Alexa Fluor 594 conjugate, FITC-goat anti-rabbit IgG
(H+L) secondary antibody, BODIPY FL C_5-ganglioside GM1,
CholEsteryl 4,4-difluoro-5-(4-methoxyphenyl)-4-bora-3a,4a-diaza-
s-indacene-3-undecanoate, and Di-4-ANEPPDHQ were from

ThermoFisher Scientific. Anti-cholera toxin B subunit (B040M)
was from GeneTex, Inc. Anti-Akt1/PKBα (AW24), Wmn, and
protease inhibitor mixture set III were from EMD Millipore.
Anti–caveolin-3 was from Novus Biologicals. Anti-klotho (KM2076)
was from TransGenic, Inc. Anti–phospho-Akt (Ser473 and Thr308)
were from Cell Signaling Technology. Anti–caveolin-1 (N-20),
anti-CD71 (H-300), and horseradish peroxidase conjugated second-
ary antibodies were from Santa Cruz Biotechnology. All phos-
phoinositides, BODIPY-C_{16}-PtdIns(4,5)P_2, tetramethylrhodamine
(TMR)-C_{16}-PtdIns(4,5)P_2, and carriers (Histone H1) were from
Echelon Biosciences.

**Isolation of Lipid Rafts from HeLa Cells and Mouse Heart by Sucrose
Gradient Ultracentrifugation.** HeLa cells were maintained at 37 °C
under a 5% (vol/vol) CO_2 atmosphere in DMEM (ThermoFisher
Scientific) supplemented with 100 units/mL penicillin and 100 μg/mL
streptomycin, 10% (vol/vol) FBS, and 1 mM sodium pyruvate
(Sigma-Aldrich). For cell preparation and isolation of lipid rafts
(29), HeLa cells were grown to confluence in two 100-mm culture
dishes. Cells were washed three times with ice-cold PBS (2.7 mM
KCl, 137 mM NaCl, 1.8 mM KH_2PO_4, and 10 mM Na_2HPO_4,
pH 7.4). Upon completion of the PBS wash, 2 mL of ice-cold
detergent lysis (DL) buffer (10 mM Tris·HCl, pH 7.4, 1 mM
EDTA, 0.5 mM EGTA, 250 μM Na orthovanadate, 1 mM Na
fluoride, 1% Triton X-100, and protease inhibitor mixture) was
added to one cell culture dish for 1 min on ice. After 1 min in DL
buffer, cell lysates were removed by scraping and were transferred
sequentially to the second dish for 1 min on ice. Cell lysates or
dissected mouse hearts (from klotho-deficient mice and wild-type
littermates) were transferred to a 2-mL loose-fitting Dounce ho-
mogenizer for 20 min on ice. Homogenization was then carried
out with 10 strokes of the homogenizer on ice. The homogenates
were transferred into the bottom of a 12-mL ultracentrifuge tube
and were adjusted to 40% (wt/vol) sucrose by addition of an
equal volume of 80% (wt/vol) sucrose in DL buffer. A discon-
tinuous sucrose gradient was generated by overlaying with 4 mL
of 30% (wt/vol) sucrose in DL buffer and 4 mL of 5% (wt/vol)
sucrose in DL buffer. The solution was then centrifuged at
210,000 × *g* for 20 h at 4 °C in an SW 41 Ti rotor (Beckman
Coulter). At completion of centrifugation, a faint light-scattering
band consisting of lipid raft/caveolar material was observed at the
5% sucrose–30% (wt/vol) sucrose interface. Twelve 1-mL fractions
were collected from the top of the tube. Aliquots of each fraction
were precipitated with prechilled acetone at −20 °C for 1 h. Pre-
cipitates were collected by centrifugation and pellets were washed
twice with acetone. The supernatant was removed and the re-
maining acetone was allowed to evaporate. Pellets were resus-
pended in 1× Laemmli's sample buffer [62.5 mM Tris·HCl, pH 6.8,
2% SDS, 10% (vol/vol) glycerol, 0.002% bromophenol blue, and
100 mM DTT] and stored frozen until ready for analysis by SDS/
PAGE gel electrophoresis. For GM1 staining, each fraction was
dot-blotted on PVDF membranes and probed with cholera toxin
subunit B-Alexa Fluor 594 conjugate and anti-cholera toxin B
subunit antibodies. Dot blots were then incubated with secondary
antibodies conjugated to horseradish peroxidase for 1 h at room
temperature and visualized by enhanced chemiluminescence.

Immunofluorescence Staining, Imaging, and Image Analysis. HeLa
cells were allowed to adhere to poly-L-lysine–coated coverslips
overnight at 37 °C. Following treatment with klotho or MβCD
at 37 °C, cells were rinsed with ice-cold PBS three times and
incubated with 1 μg/mL cholera toxin subunit B-Alexa Fluor 594

conjugate on ice for 20 min. For double immunofluorescence staining of endogenous GM1 with exogenous GM1 ganglioside, cells were rinsed with ice-cold PBS three times and incubated with 50 nM BODIPY-FL-C$_5$-GM1 on ice for 5 min. After washing with ice-cold PBS, the cells were immediately fixed with 4% (wt/vol) paraformaldehyde (PFA) for 15 min at room temperature. For double immunofluorescence staining of endogenous GM1 ganglioside with caveolin-1 or CD71, cells were stained with cholera toxin subunit B-Alexa Fluor 594 conjugate as described. After fixation with 4% PFA, cells were rinsed with PBS, blocked, and stained with anti–caveolin-1 (N-20) or anti-CD71 (H-300) for 1 h at room temperature. Following PBS washing steps, secondary antibody staining was performed with FITC-conjugated goat anti-rabbit IgG. Coverslips were then washed with PBS and mounted in ProLong Gold antifade reagent (ThermoFisher Scientific). Images were acquired and processed using a Zeiss LSM510 laser scanning confocal microscope system with a Zeiss 63× oil-immersion objective. Quantitative colocalization analysis of confocal fluorescence microscopy images was carried out using ImageJ software with the colocalization threshold plugin (30).

Biolayer Interferometry. Biolayer interferometry is a technology that detects association of an analyte to a ligand that is immobilized to an optical sensor. Association leads to a change in the interference pattern of the light reflected from the end of the sensor, which is translated directly into the thickness of the bound layer of analyte. Biolayer interferometry was performed using the Octet Red384 system with ForteBio Octet analysis software (ForteBio). Measurement buffer consisted of a 10/1 (vol/vol) mix of 1× kinetics buffer (18-1092; Fortebio) with 50% (vol/vol) glycerol, 0.1 mM EDTA, and 20 mM MES. In each measurement, streptavidin sensors were uncoated in measurement buffer for 15 min, loaded with 150 nM biotin, biotindiol, or biotinylated glycan for 4 min followed by incubation with fresh klotho solution at 30 °C for 400 s and dissociation for 500 s. Biotindiol served as reference. The data were processed by subtraction of the signal for biotindiol, alignment to association, interstep correction to dissociation, and Savitzky–Golay filtering to result in the given sensorgram. The respective values for k_{on}, k_{off}, and K_d were determined by analyzing association and dissociation in a 1:1 model, full local fitting. For a confident determination of the K_d, different concentrations of klotho were bound to either biotinylated 3′-sialyllactose or biotindiol. The resulting binding curves were processed and analyzed as described above, using biotindiol at a given concentration of klotho as reference for 3′-sialyllactose with the same concentration of klotho. Equilibrium response (R_{eq}) was plotted over concentration of klotho and the K_d was determined using the following equation for the model of site specific binding to one site: $R_{eq} = (R_{max} \times \text{concentration})/(K_d + \text{concentration})$.

Isolating of Cardiac Ventricular Myocytes from Mice with Induced Hypertrophy. To induce cardiac hypertrophy, mice were administrated isoproterenol (3 mg/kg s.c.) daily for 15 d. Hypertrophied hearts were removed, perfused retrograde via the aorta with a solution containing (in millimolar) 113 NaCl, 4.7 KCl, 1.2 MgSO$_4$, 0.6 KH$_2$PO$_4$, 0.6 Na$_2$HPO$_4$, 10 NaHCO$_3$, 30 taurine, 5.5 glucose, 10 2,3-butanedione monoxime, and 10 Hepes (at pH 7.4), followed by a solution containing in addition 1 mg/mL type-2 collagenase and 0.1 mg/mL protease XIV as described (9). The perfusion solution was maintained at 37 °C and equilibrated with 100% O$_2$. Thereafter, the ventricle was removed, chopped into small pieces, and further digested in the enzyme solution. Enzyme digestion was stopped by adding 2.5% (wt/vol) BSA and 0.1 mM CaCl$_2$. The tissue–cell mixture was filtered through a sterilized-gauze sponge, centrifuged using a tabletop centrifuge at $50 \times g$ for 1 min. The resulting cell pellet was resuspended in the stopping buffer and [Ca^{2+}] titrated to 0.5 mM by addition of

100 mM CaCl$_2$ stock solution in four steps over 20 min. Isolated myocytes were stored at room temperature until use.

Electrophysiological Recordings of TRPC6 Currents. HEK293 cells (control or expressing recombinant TRPC6) or freshly isolated cardiac myocytes were voltage-clamped in ruptured whole-cell mode with an Axopatch 200B patch-clamp amplifier and Pulse software (Axon instruments Inc.) as previously described (9). Cells were continuously perfused with bath solution. Cells were held at 0-mV membrane potential (at −20 mV for recording cardiac myocyte) and stimulated with repetitive ascending ramp pulse from −100 mV to +100 mV for 400 ms every 10 s (or descending from +80 mV to −100 mV for 500 ms every 10 s for cardiac myocyte). The pipette and bath solution for recording HEK293 cells contained (in millimolar) 140 CsCl, 1 MgCl$_2$ 1.5 CaCl$_2$, 2 ATP-Mg, 5 EGTA, 10 Hepes (pH 7.2 with CsOH) and 140 NaCl, 0.5 EGTA, 10 Hepes, 10 glucose, and 10 mannitol (pH 7.4 with NaOH), respectively. The pipette and bath solution for recording cardiac myocytes contained (in millimolar) 9.4 NaCl, 120 CsCl, 1 MgCl$_2$ 3.5 CaCl$_2$, 0.2 GTP-Na, 10 BAPTA, 10 Hepes (pH 7.2 with CsOH) and 140 NaCl, 5 CsCl, 1 MgCl$_2$, 10 glucose, and 10 Hepes (pH 7.4 with NaOH), respectively. For recording cardiac myocytes, bath solution also contained 1 μM of nifedipine and 3 mM of NiCl$_2$ to block current flow through L-type Ca^{2+} channel and Na$^+$/Ca^{2+} exchanger, respectively. The resistance of electrodes containing pipette solution was 1.5 ~ 3 MΩ. TRPC6 currents were activated by bath application of 1-oleoyl-2-acetyl-sn-glycerol (OAG, 100 μM), low-pass-filtered at 2 kHz, and sampled every 0.1 ms (10 kHz). Data acquisition and analysis were performed using pClamp9.2 program (Axon Instrument Inc.) and Prism (V3.0) software (GraphPad Software).

_GP_ Measurements. HEK293 cells were grown onto 35-mm glass-bottom dishes (MatTek Corp.) to 70% confluency. Experimental cells were shifted to phenol-free media (DMEM/F-12 media with 10% FBS, 15 mM Hepes, 2.5 mM L-glutamine, 100 U/mL penicillin, and 100 U/mL streptomycin) 1 h before imaging. Di-4-ANEPPDHQ (2 μM final concentration) was added to the media and incubated for 5 min at 37 °C. When indicated, klotho was added at the same time with di-4-ANEPPDHQ. Glucose oxidase from _Aspergillus niger_ (MP Biomedical), catalase from bovine liver (Fisher), 200 U/mL glucose oxidase, and 0.04 mg/mL catalase (1,404 U/mL) were added to the media right before imaging to reduce the phototoxic effect of the dye. Live-cell images were obtained using Zeiss 780 laser-scanning confocal/multi-photon-excitation fluorescence microscope with a 34-channel GaAsP QUASAR detection unit and nondescanned detectors for two-photon fluorescence (Zeiss). The imaging settings were initially defined empirically to maximize the signal-to-noise ratio and to avoid saturation, and they were kept constant for all measurements for comparative imaging and results. Images (focusing at the basal part of the cells, 5 s per image) were acquired beginning at 5 min after incubation with di-4-ANEPPDHQ ± klotho via a Zeiss C-Apochromat 40×/1.2 N.A. Korr FCS M27 water-immersion lens objective. The definite focus mechanism was implemented to maintain the same focal plane over the whole image acquisition period. One percent of a 30-mW Argon laser was used for excitation at 488 nm, and emission signals corresponding to the ordered and disordered phases were detected simultaneously through two spectral channels, Ch1 [508–588 nm (ordered)] and Ch2 [615–695 nm (disordered)]. Image processing was performed using Zeiss ZEN 2012 software. The series of images were analyzed in ImageJ software. The two channels were thresholded and made binary masks and then multiplied by each corresponding channel to account for membranes only. The thresholded Ch2 was then multiplied by a calibration factor, G-factor. At each pixel, GP values were calculated using the equation $GP = I_{508–588} - G*I_{615–695}/I_{508–588} + G*I_{615–695}$, where

$I_{508-588}$ and $I_{615-695}$ are intensity values from the ordered (Ch1) and disordered (Ch2) channels, respectively (22). The G-factor was calculated from the formula $G = I_{508-588}*(1 - GP_{ref.})/I_{615-695}*(1 - GP_{ref.})$, where $GP_{ref.}$ is the GP value of the di-4-ANEPPDHQ in a solution measured by the spectrofluorometer, and $I_{508-588}$ and $I_{615-695}$ are the mean intensity values of Ch1 and Ch2 images (taken from their corresponding histograms) of the dye in a solution taken by the microscope using the same microscope settings used while taking the time series images. The average G-factor value 1.106, determined from three separate measurements) was used to calculate the mean GP from the original raw data in this study. Mean GP values were set to a range between −0.99 and 0.99.

FLIM-FRET Studies. HEK cells were stained (at room temperature for 5 min) with BODIPY FL-505/510-C_5-Ganglioside GM1 (donor, 100 nM) and with or without CholEsteryl BODIPY 542/563-C_{11} (acceptor, 400 nM). Basic FLIM microscopy was done as described above. For FLIM-FRET studies, a dichroic filter (488 nm, Di02-R488-25-D; Semrock Inc.) was used to separate the fluorescence signal, which was then detected by a 506- to 594-nm (Semrock Inc.) emission filter that was placed in front of the detector (GM1-cholesterol FLIM-FRET). A dichroic filter (594-nm, Di02-R594-25-D; Semrock Inc.) was used to reflect the fluorescence signal into a 506- to 594-nm (Semrock Inc.) filter that was placed in front of the detector (GM1-klotho FLIM-FRET). The two-photon excitation was blocked by a two-photon emission filter. Images of the basolateral membrane were obtained in the 256 × 256 format with a pixel dwell time of 12.61 µs per pixel and averaging

over 30 frames. VistaVision software by ISS was used for the acquisition and analysis of FLIM images. A digital-frequency-domain setup measured the modulation and phase at each pixel within an image. For analysis using the phasor diagram, the modulation (m) and phase (φ) determined the radial and angular coordinate, respectively (12, 31). G and S values in the phasor plot were calculated according to the following equations: G = m* cos (φ); S = m* sin (φ). The phasor of the unquenched donor was determined as the phasor of cells stained only with BODIPY-GM1. The phasor of the background was determined as the phasor of the autofluorescence signal from unstained cells. To examine FRET occurrences, shifts of the donor–acceptor vs. donor only phasors were determined. The trajectory of variable FRET efficiencies was drawn in the plot. The position that donor was quenched in the presence of acceptor yields the value of efficiency associated with the FRET interaction.

MEND. MEND responses in HEK293 cells were determined as described (27). Klotho (1 nM) was applied to cells after removal from culture dishes. Upon dispersion into the recording chamber the klotho concentration was decreased to 0.1 nM.

Statistical Analysis. Each experiment was repeated at least once with similar results. Data are presented as mean ± SEM. Statistical comparison between two groups of data were made using two-tailed unpaired Student's t test. Multiple comparisons were determined using one-way analysis of variance followed by Tukey's multiple comparison tests.
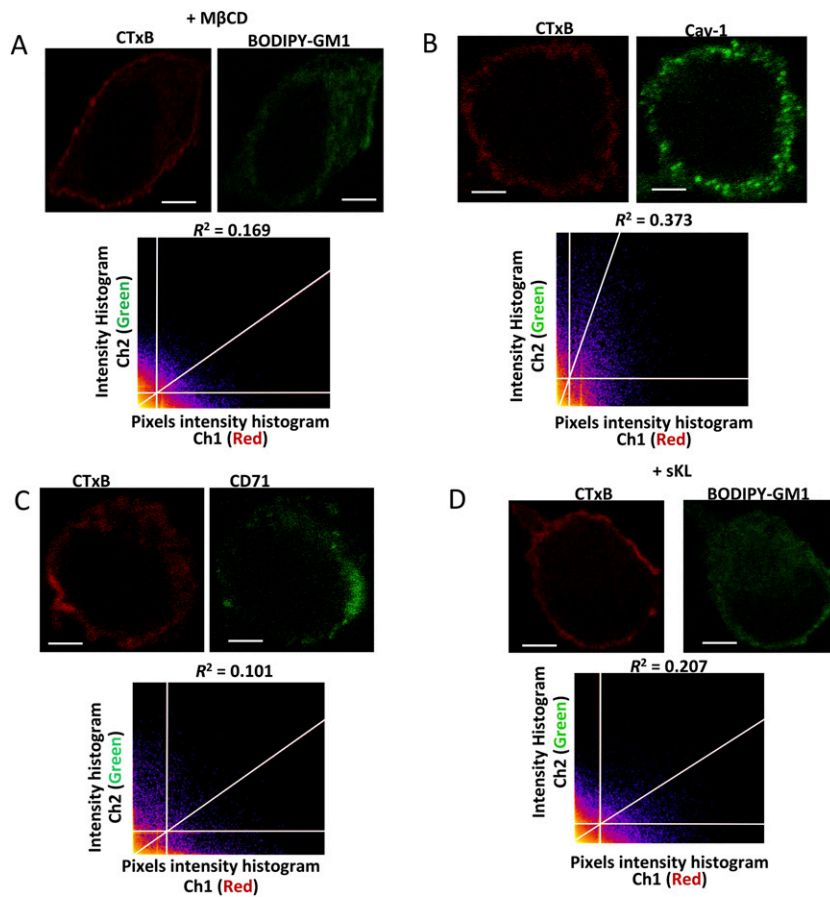
Fig. S1. (*A–D*) Representative images and Pearson's coefficient showing colocalization of CTxB/Cav-1, no colocalization for CTxB/CD71, and effect of MβCD or sKL treatment on CTxB/BODIPY-GM1 colocalization. Note that fluorescence intensity of CTxB-Alexa Fluor 594 in cells treated with sKL is reduced by ~11% compared with without klotho treatment, due to the fact that sKL binds sialic acids of gangliosides and competes for CTxB binding (Fig. 3 and Fig. S6). The mild reduction in CTxB-labeled fluorescence intensity does not affect Pearson's correlation coefficient because the analysis is based on correlation between green and red channel pixel intensity histogram and is independent of absolute fluorescence intensity. (Scale bars, 5 μm.)
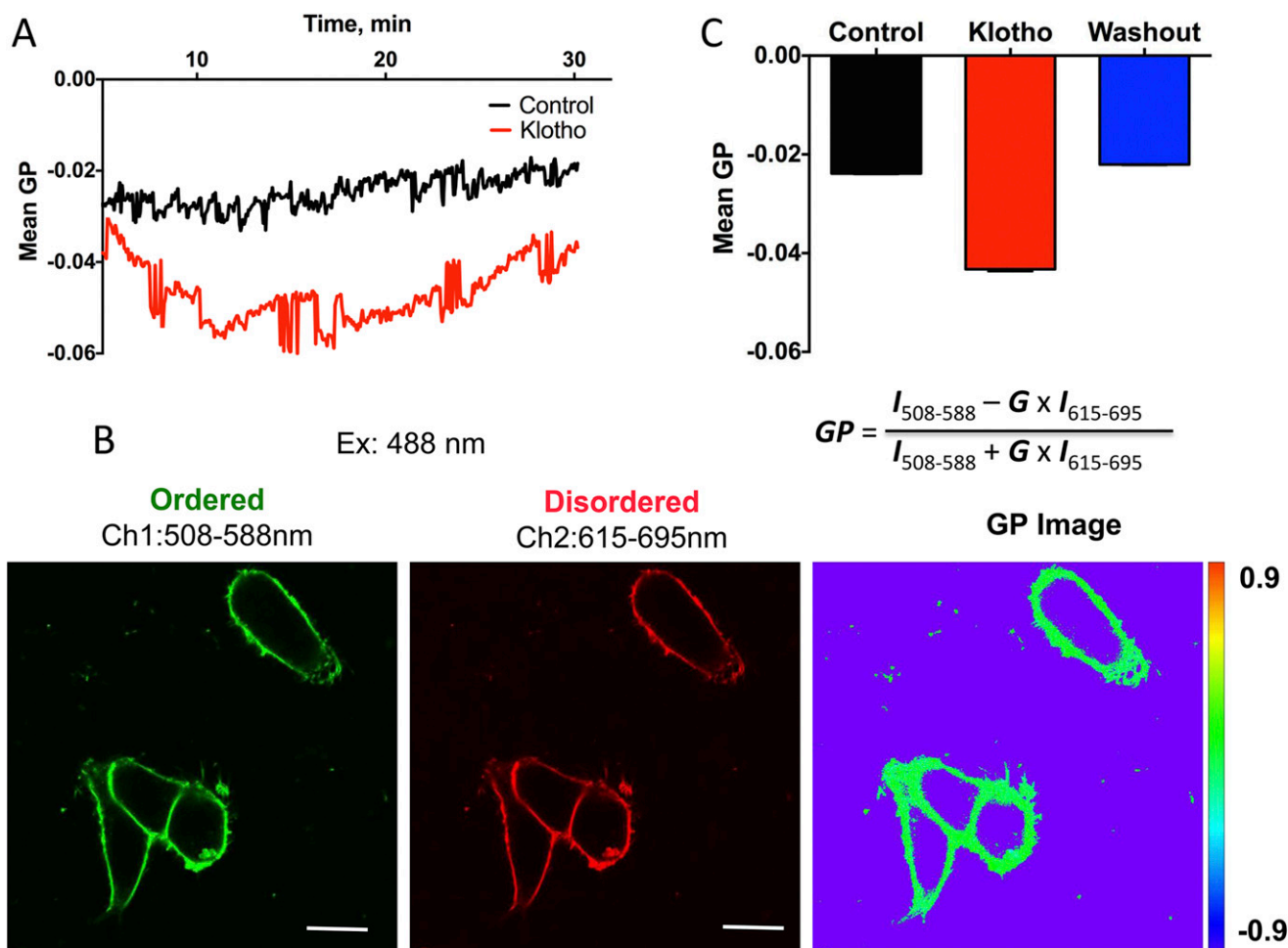
Fig. S2. Klotho decreases membrane order analyzed by using a polarity-sensitive membrane probe. (*A*) Cells were incubated with ANEPPDHQ (2 μM) ± klotho (300 pM) for 5 min at 37 °C before imaging (5 s per image consecutively for total 300 images over the subsequent 25 min). Line plots show mean *GP* values for 300 single images over time. Heat-inactivated klotho (70 °C for 10 min) had no effects on *GP* values. (*B*) *GP* was calculated by ratiometric measurement of the fluorescence intensity recorded in two spectral channels using the equation shown. (Scale bars, 20 μm.) (*C*) Bar graph shows reversibility of *GP* (taken at 30 min) after washout of sKL.

$$GP = \frac{I_{508-588} - G \times I_{615-695}}{I_{508-588} + G \times I_{615-695}}$$
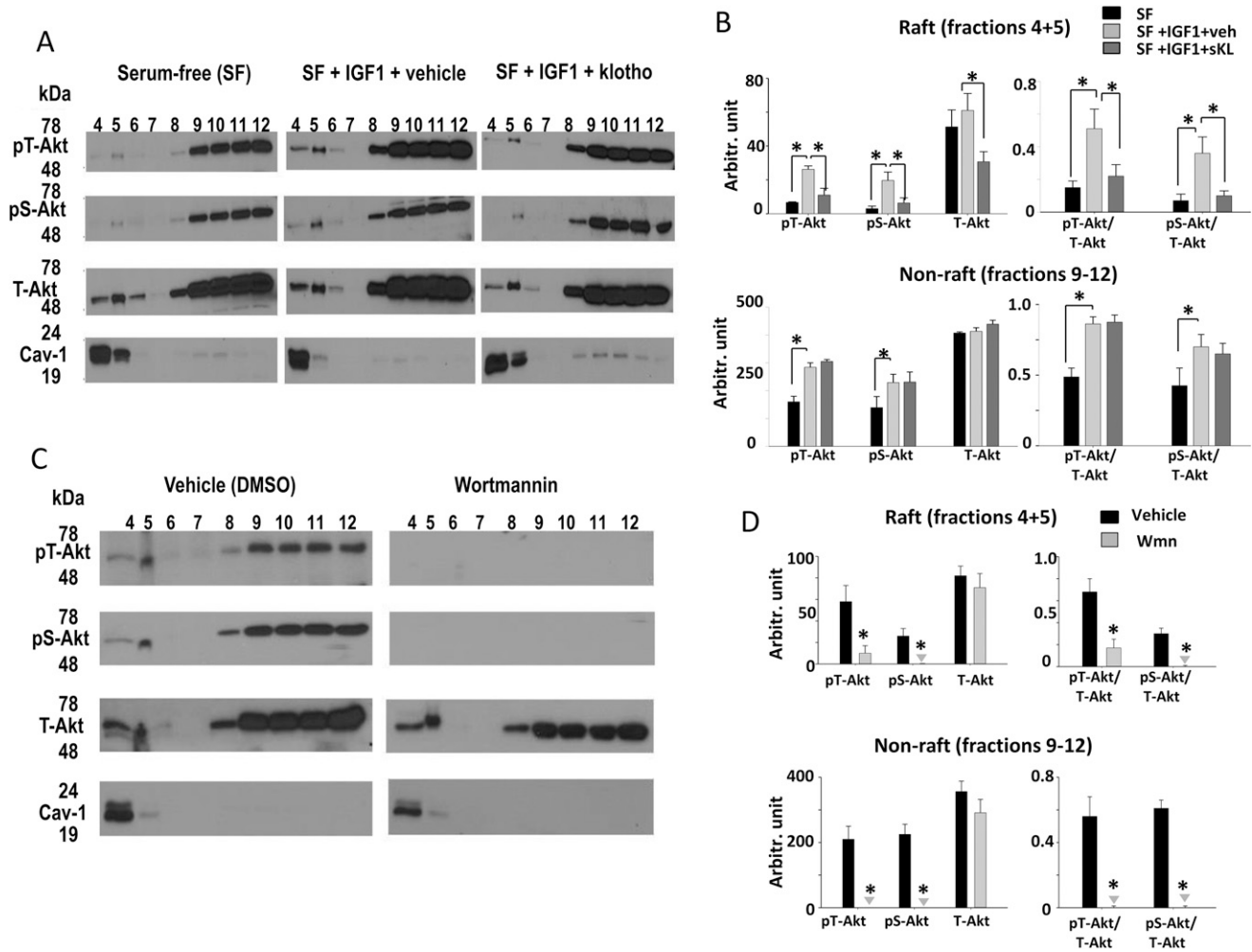
Fig. S3. Effect of sKL and Wmn on growth factor-driven PI3K/Akt signaling. (*A* and *B*) HeLa cells grown in serum-containing medium were serum-starved for 24 h, pretreated with sKL or vehicle, and stimulated by IGF1 (26 nM) for 5 min. *A* shows one representative experiment. *B* shows mean ± SEM from 3 separate experiments. *$P < 0.05$ between indicated groups. (*C* and *D*) PI3K inhibitor Wmn (100 nM for 2 h) abrogates PI3K/Akt signaling in lipid rafts (fractions 4 and 5) and nonraft membrane (fractions 9–12). Confluent HeLa cells grown in serum-containing medium were treated with vehicle or Wmn before lysis in an ice-cold detergent lysis buffer containing 1% Triton X-100 and subjected to sucrose gradient ultracentrifugation. pT-Akt, phosphorylation of Akt at Thr-308; pS-Akt, at Ser-473. T-Akt indicates total Akt. *A* shows one representative experiment. *B* shows mean ± SEM from four separate experiments. *$P < 0.01$, vehicle vs. Wmn. The inverted triangle indicates bar height not visible. Note that virtually all cellular proteins including cytosolic proteins and Triton X-100–soluble plasma membrane and inner organelle proteins are distributed in the nonraft regions. Because nonraft membranes include the bulk of cell membranes and intracellular organelles, the total abundance of proteins in nonraft membrane fractions is >300-fold higher than in raft regions. This fact explains why the unnormalized abundance of Akt (not normalized to protein density) in nonraft regions is approximately fivefold more than in raft regions (see quantitation in Fig. 2*B*). In our studies, we presented unnormalized results given that normalized Akt signals are below detection.
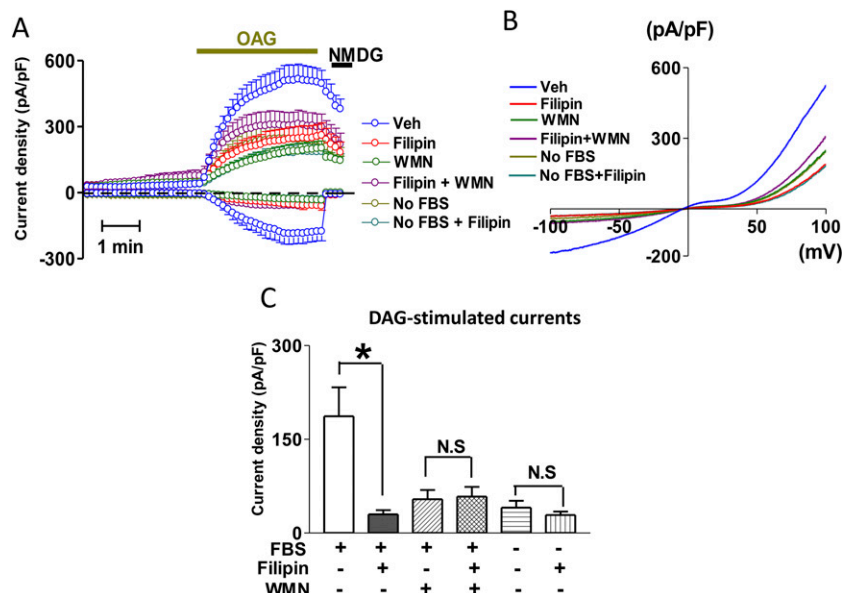
Fig. S4. Evidence for important role of raft-associated PI3K signaling in DAG-stimulated TRPC6 channel activity. (A) Time course of DAG-stimulated currents. Confluent cells expressing TRPC6 channels were either serum-starved for 24 h or not starved and incubated with or without filipin (10 μg/mL for 1 h) or Wmn (200 nM for 30 min) before recording. Ruptured whole-cell TRPC6 currents in response to repetitive ascending voltage ramp (−100 mV to +100 mV for 400 ms every 10 s) were recorded. After 2–3 min, OAG, a membrane-permeant analog of DAG (100 μM), was added to the bath solution to activate TRPC6 currents. Basal currents before addition of OAG were not significantly different from untransfected cells. At the end of experiments, the bath solution was replaced by a solution containing nonpermeant cation N-methyl-D-glucamine (NMDG) to assess TRPC6-mediated inward currents. Circles and error bars represent mean ± SEM (n = 7–14 cells recorded for each group). (B) Representative current–voltage relationship curves of peak currents. (C) DAG-stimulated inward TRPC6 current density shows no additivity between inhibition of TRPC6 by filipin, Wmn, or serum-deprivation, indicating that DAG stimulation of TRPC6 channel activity requires a cholesterol-dependent, serum-stimulated PI3K signaling pathway. NS, not significant.
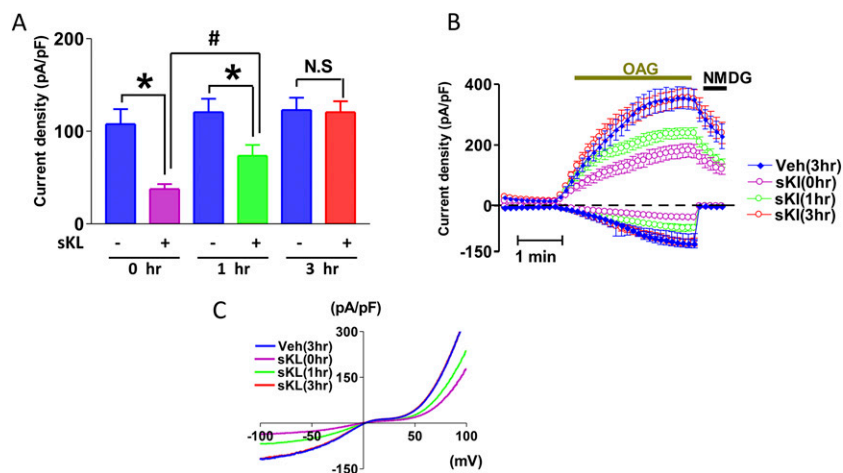
Fig. S5. Reversibility of klotho inhibition of TRPC6 after klotho washout. (A) Cells expressing TRPC6 were treated with or without sKL (300 pM) in serum medium overnight. Cells were washed three times using PBS to remove klotho. Cells were recorded for DAG-stimulated TRPC6 currents immediately after washout (0 h) or incubated in serum-free medium + IGF1 (13 nM) at 37 °C for 1 h or 3 h before recording. Data are mean ± SEM of inward TRPC6 current density (n = 8–12 cells recorded for each group). *P < 0.01 between indicated groups. #P < 0.05 between indicated groups. After klotho washout, the 1- to 3-h delay in the recovery of DAG-stimulated TRPC6 currents back to the level without klotho treatment is probably due to the time required for lipid rafts to reform, for PI3K/Akt to reassociate with rafts, and for PI3K/Akt signaling to prime TRPC6 vesicles for stimulated exocytosis by DAG. Note that whereas sKL affects lipid rafts in 5–10 min (Fig. 1), given the mechanism for PI3K to regulate TRPC6 exocytosis is unknown and that it will take time for PI3K's effect to subside after inhibition by klotho, we treated cells with sKL for 3 h before recording of TRPC6. Inhibition of TRPC6 is reversible upon klotho washout, which supports the notion that the effect is not mediated by uptake and intracellular action of klotho. NS, not significant. (B) Time course of DAG-stimulated currents. (C) Current–voltage relationship curves of peak TRPC6 currents.
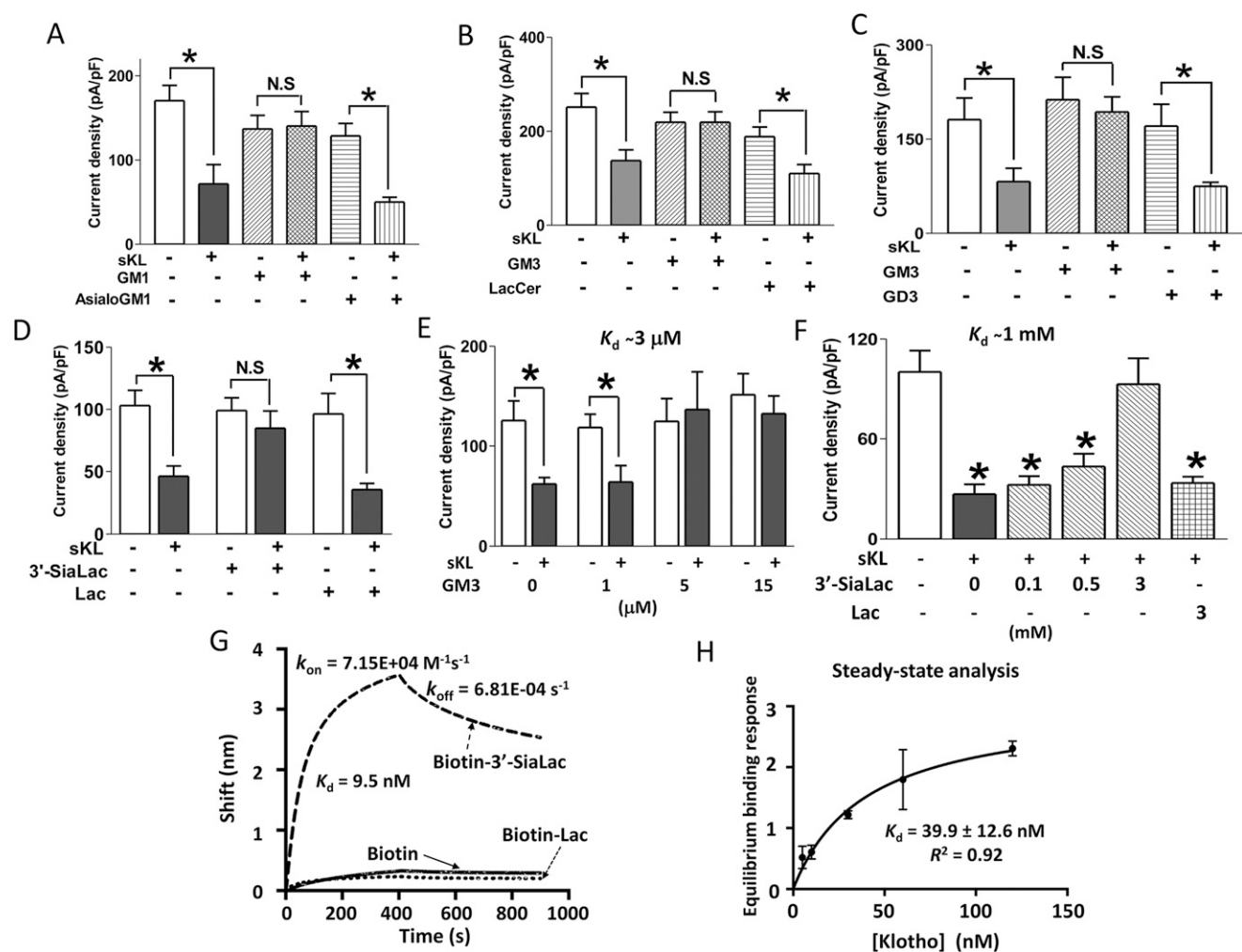
Fig. S6. Structural determinants of GM1 and GM3 for klotho binding and inhibition of lipid raft-associated PI3K/Akt signaling and TRPC6 channel activity. (*A*) sKL (300 pM final concentration) was mixed with GM1 or asialo-GM1 (17 μM final concentration) in 1 mL cell culture medium for 1 h. Cells were incubated with the mixture medium at 37 °C for 3 h before recording. In control experiments, medium contains no sKL with or without GM1 or asialo-GM1. n = 10–14 each group. *P < 0.01 between indicated groups. (*B*) Experiments as in *A* except that GM3 or LacCer was used. n = 11–13 each group. *P < 0.01 between indicated groups. (*C*) Experiments as in *A* except that GM3 or GD3 was used. n = 15–17 each group. *P < 0.01 between indicated groups. (*D*) Experiments as in *A* except that 3′-sialyllactose (3′-SiaLac) or lactose (Lac) was used. n = 13–16 each group. *P < 0.01 between indicated groups. (*E*) Dose–response curve for competition of klotho's effect by GM3. Apparent K_d for GM3 estimated at 3 μM. (*F*) Dose–response curve for competition of klotho's effect by α2-3-sialyllactose. Apparent K_d for free α2-3-sialyllactose estimated at 1 mM. (*G*) Spectral shifts of reflected light due to changes in biosensor thickness (Δλ, in nanometers) were measured following 170 nM klotho binding to streptavidin sensors loaded with 150 nM biotin-labeled α2-3-sialyllactose, lactose, or only biotin against biotindiol reference. One of two experiments is shown. (*H*) Steady-state maximal binding at different concentrations of klotho was performed. Equilibrium binding constant (K_d) calculated from dose–response studies assuming one specific binding site is 39.9 ± 12.6 nM (mean ± SEM; n = 14 individual data points) and agrees with the K_d value calculated based on the ratio of off-rate constant (k_{off}) over on-rate constant (k_{on}). NS, not significant.

Fig. S7. Dose–response curve for competition of klotho's effect by α2-6-sialyllactose. (*A*) Cells expressing TRPC6 were treated with sKL (300 pM final concentration) premixed with α2-6-sialyllactose (6′-SiaLac) at different concentrations. In control experiments, medium contains no sKL. Data are mean ± SEM of inward TRPC6 current density (*n* = 10–13 cells recorded for each group). *$P < 0.01$ vs. no sKL. (*B*) Time course of DAG-stimulated currents. (*C*) Current–voltage relationship curves of peak TRPC6 currents.

Fig. S8. Klotho blunts MEND (massive endocytosis) of surface membrane but does not cause global membrane disorder. (*A*) Representative record of MEND. Membrane capacitance, a measurement of cell membrane area (blue trace, in picofarads), and membrane current (red trace, in nanoamperes) were measured by patch-clamp recording. After Ca^{2+} influx was activated by applying 2 mM external Ca^{2+} for 10 s in the presence of 40 mM cytoplasmic Na^+, MEND amounted to more than 40% of the surface membrane. (*B*) Incubation of cells with klotho decreased MEND by more than 60%. Depletion of ceramide-dependent gangliosides by NB-DGJ (25 μM, overnight) did not decrease MEND but ablated the ability of klotho to inhibit MEND. Data represent mean ± SEM *$P < 0.05$, * *$P < 0.01$ between indicated groups. (*C*) Representative record of hexyltriphenylphosphonium (C6TPP) permeation experiments. Membrane capacitance (red trace, in picofarads) and inward current (blue trace, in picoamperes) were measured by patch-clamp recording. Extracellular applications of C6TPP generated reversible inward currents. (*D*) Klotho treatment does not affect C6TPP-dependent inward currents.